

TEXT-PROMPTABLE PROPAGATION FOR REFERRING MEDICAL IMAGE SEQUENCE SEGMENTATION

Runtian Yuan¹ Jilan Xu¹ Mohan Chen¹ Qingqiu Li¹
 Yuejie Zhang^{1,*} Rui Feng^{1,*} Tao Zhang² Shang Gao³

¹Fudan University ²Shanghai University of Finance and Economics ³Deakin University

ABSTRACT

Medical image sequences, generated by both 2D video-based examinations and 3D imaging techniques, consist of sequential frames or slices that capture the same anatomical entities (e.g., organs or lesions) from multiple perspectives. Existing segmentation studies typically process medical images using either 2D or 3D methods in isolation, often overlooking the inherent consistencies among these images. Additionally, interactive segmentation, while highly beneficial in clinical scenarios, faces the challenge of integrating text prompts effectively across multi-modalities. To address these issues, we introduce an innovative task, **Referring Medical Image Sequence Segmentation** for the first time, which aims to segment the referred anatomical entities corresponding to medical text prompts. We develop a strong baseline model, Text-Promptable Propagation (TPP), designed to exploit the intrinsic relationships among sequential images and their associated textual descriptions. TPP supports the segmentation of arbitrary objects of interest based on cross-modal prompt fusion. Carefully designed medical prompts are fused and employed as queries to guide image sequence segmentation through triple-propagation. We curate a large and comprehensive benchmark covering 4 modalities and 20 different organs and lesions. Experimental results consistently demonstrate the superior performance of our approach compared to previous methods across these datasets.

1 INTRODUCTION

In the realm of medical imaging, both 2D video-based examinations, such as endoscopy and ultrasound, and 3D imaging techniques like CT and MRI, produce sequential frames or slices that capture the same anatomical entities (e.g., organs and lesions). These image sequences are not merely collections of individual snapshots but are deeply interconnected, with each frame or slice providing a unique view of the same object from different angles and in varying shapes. The consistencies among these sequential images are crucial for comprehensive medical analysis and diagnosis.

Current studies on medical image segmentation involve advanced machine learning tools designed to automatically identify and separate different organs, tissues, or pathological regions from medical images like CT scans, MRIs, and X-rays. These medical segmentation models are essential for tasks such as disease screening, organ segmentation, and anomaly detection. As depicted in Figure 1 (a-c), these models face two primary drawbacks: 1) Separate network architectures for 2D and 3D medical images. Researchers often apply distinct methodologies for 2D and 3D medical images, using 2D approaches for planar images or slices (Ronneberger et al., 2015; Chen et al., 2021) and 3D techniques for volumetric data (Milletari et al., 2016; Zhao et al., 2023). These networks neglect the consistency across temporal frames from 2D video-based examinations and sequential slices from 3D volumes when images are interrelated or part of a sequence, leading to discrepancies and sub-optimal outcomes. 2) Limitation to closed sets of categories and lack of human interactions. In multi-class segmentation tasks, existing methods (Chen et al., 2021; Zhao et al., 2022) typically restrict results to predefined classes, reducing flexibility and preventing the specification of particular classes for referring segmentation. This rigidity limits the adaptation of segmentation processes to specific clinical needs or emerging requirements in complex medical scenarios.

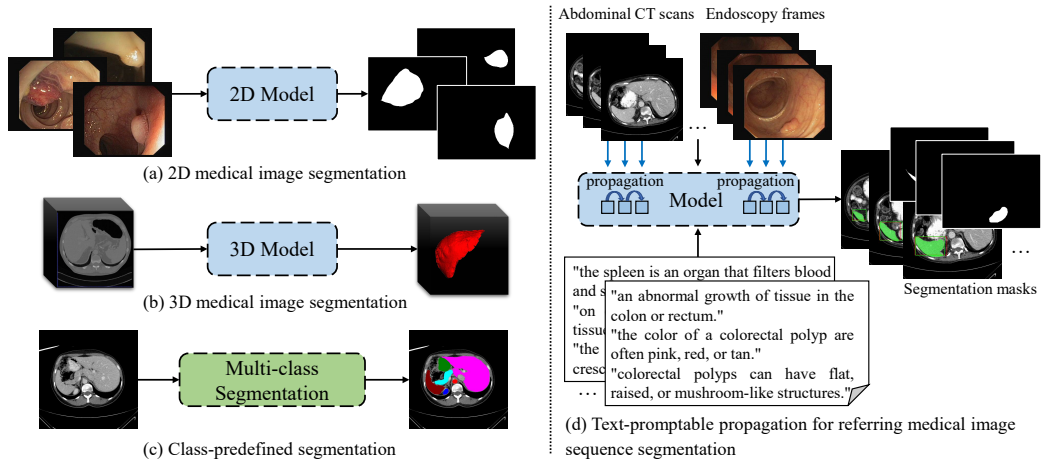


Figure 1: Medical image segmentation. (a) 2D models are often applied to 2D images or slices from 3D volumes, (b) 3D images typically utilize 3D models, (c) in multi-class segmentation tasks, once the categories are defined, the prediction results are restricted to those categories, without the ability to specify a specific category to segment, and (d) our method leverages medical text prompts to refer to target objects and treats frames from 2D video-based examinations and slices from 3D volumes as medical image sequences for segmentation. This approach enhances the flexibility and accuracy by integrating text-based references with a broader range of image data.

To address these challenges, we introduce an innovative task, **Referring Medical Image Sequence Segmentation**, which aims to identify and segment anatomical entities corresponding to given text prompts within medical image sequences. These sequences involve both temporally related frames from videos and spatially related slices in volumes. For this task, we present our **Text-Promptable Propagation (TPP)** model, a strong baseline designed to leverage the intrinsic relationships among sequential images and their associated textual descriptions. As shown in Figure 1 (d), TPP unifies frames from 2D video-based examinations and slices from 3D volumes, and supports the segmentation of arbitrary objects of interest based on text prompts.

TPP integrates two key components: 1) **Cross-modal Prompt Fusion**. This component supports medical text prompts and vision-language fusion. Medical text prompts often provide valuable knowledge and context by highlighting specific regions of interest and guiding attention. We propose cross-modal prompt fusion to integrate prompts that describe various characteristics of anatomical entities, linking medical image sequences with text prompts across vision and language modalities. This component facilitates a more comprehensive understanding of the data by combining insights from both textual and visual information. 2) **Transformer-based model with Triple Propagation**. To uniformly model the temporal relationships between 2D frames and cross-slice interactions in 3D volumes, we employ a Transformer-based encoder-decoder architecture that incorporates propagation strategies to track the referred objects throughout the sequences.

We curate a large dataset for referring medical image sequence segmentation, Ref-MISS, by prompting Large Language Models and re-organizing public medical datasets. Ref-MISS is sourced from 18 diverse medical datasets across 4 modalities, including MRI, CT, ultrasound, and endoscopy. It covers 20 different organs and lesions from various regions of the body, as illustrated in Figure 2.

2 RELATED WORK

Medical Image Segmentation. As mentioned earlier, researchers typically apply distinct methods for 2D (Ronneberger et al., 2015) and 3D (Çiçek et al., 2016; Milletari et al., 2016) medical images. 2D models are used for planar images or slices, while 3D models are intended to learn volumetric features. Isensee et al. (2021) introduced a versatile, self-adaptive deep learning framework specifically designed for medical image segmentation tasks, extending the U-Net architecture and its 3D version. Chen et al. (2021) pioneered the combination of Transformer-based architecture with Convolutional Neural Networks (CNNs) for medical image segmentation, applying a slice-by-slice

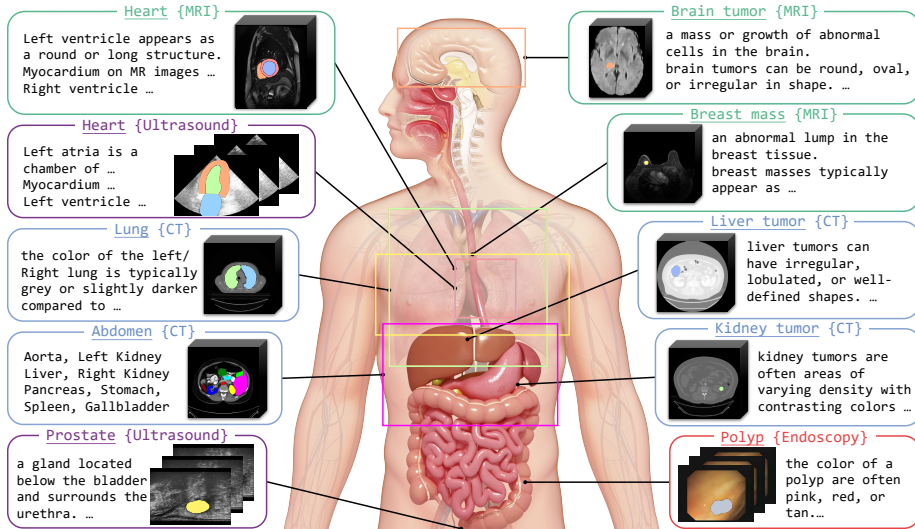


Figure 2: An illustration of focus areas in Ref-MISS dataset.

inference on 3D volumes without considering interrelationships among slices. Some works (Ji et al., 2021; Painchaud et al., 2022; Lin et al., 2023) utilize spatial-temporal cues to enhance segmentation performance; however, these models are limited to specific modalities and tasks.

Medical Vision Language Models. Medical vision language models have achieved success across multiple downstream tasks, including diagnosis classification (Moon et al., 2022; Wang et al., 2022; Tiu et al., 2022; Lu et al., 2023), lesion detection (Qin et al., 2023; Huang et al., 2024), image segmentation (Zhao et al., 2023; Li et al., 2023), report generation (Yan & Pei, 2022; Bannur et al., 2023), and visual question answering (Singhal et al., 2023; Moor et al., 2023). Qin et al. (2023) designed auto-generation strategies for medical prompts and transferred large vision language models for medical lesion detection. Zhao et al. (2023) built a model based on Segment Anything Model (Kirillov et al., 2023) in medical scenarios driven by text prompts, but the model focused on 3D medical volume segmentation and failed to account for the sequential relationships between scans. Based on our current understanding, we are the first to treat 2D and 3D medical images as unified medical image sequences, using medical text prompts to specify segmentation targets.

Referring Video Object Segmentation. Gavriluyk et al. (2018) were the first to propose inferring segmentation from a natural language input, extending two popular actor and action datasets with natural language descriptions. Seo et al. (2020) constructed the first large-scale referring video object segmentation (RVOS) dataset and proposed a unified referring video object segmentation network. Wu et al. (2022) and Botach et al. (2022) presented Transformer-based RVOS frameworks, enabling end-to-end segmentation of the referred object. Wu et al. (2023) designed explicit query propagation for an online model. Luo et al. (2024) aggregated inter- and intra-frame information via a semantic integrated module and introduced a visual-linguistic contrastive loss to apply semantic supervision on video-level object representations. Inspired by these works, we introduce a new task termed Referring Medical Image Sequence Segmentation. We process both 2D and 3D medical data into image sequences and perform an in-depth exploration of clip-level consistency within the sequences under the guidance of linguistic prompts.

3 METHOD

Given T frames or slices $\{I_t \in \mathbb{R}^{3 \times H \times W}\}_{t=1}^T$ from a medical image sequence clip and N_p medical text prompts $\{P_i\}_{i=1}^{N_p}$, the model aims to predict the segmentation masks $\{\hat{m}_t \in \mathbb{R}^{H \times W}\}_{t=1}^T$ of the referred object corresponding to the prompts. We provide an automatic text-promptable schema for referring medial image sequence segmentation. The overall architecture of our framework is illustrated in Figure 3 (a). This framework comprises vision-language fusion (Section 3.1), unified sequential processing (Section 3.2), and the training and inference procedures (Section 3.3).

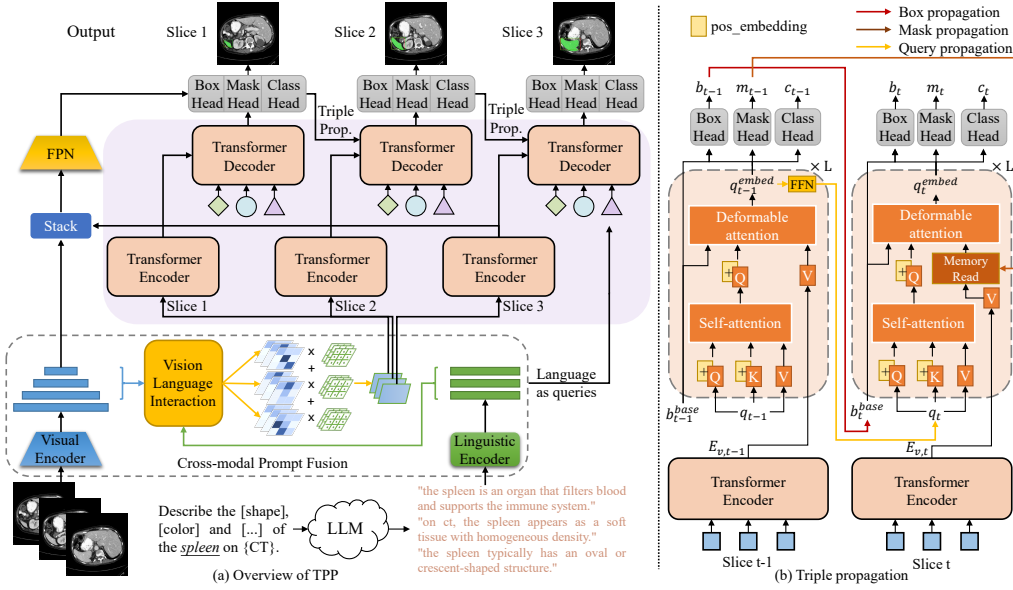


Figure 3: (a) Overall architecture of our Text-Promptable Propagation for referring medical image sequence segmentation. Triple Prop. is short for Triple Propagation. (b) Illustration of Triple Propagation in Transformer decoder, consisting of box-level, mask-level, and query-level propagation. Line from $E_{v,t-1}$ to Memory Read block is omitted for simplicity.

3.1 VISION-LANGUAGE FUSION

Prompt Acquisition. We adopt large language models to automatically generate medical text prompts. The instruction template is as follows: “You are a medical expert. Describe the [attribute 1], [attribute 2], ..., and [attribute N_p] of the *anatomical entity* on {modality} in one sentence each.” Using this template, we obtain N_p prompts for the target object (i.e., anatomical entity) that is expected to be segmented. Here, N_p is set to 3, with [attribute 1]=[profile], [attribute 2]=[shape], and [attribute 3]=[color]. The attribute [profile] conveys the characterization of organ functions and the definition of lesions, while attributes [color] and [shape] provide detailed descriptions of the morphological aspects of the object.

Feature Extraction. Image clips $\{I_t\}_{t=1}^T$ and medical text prompts $\{P_i\}_{i=1}^{N_p}$ are fed into a visual encoder and a linguistic encoder separately to extract visual features F_v for each image and textual features F_p for each prompt. F_v is a set of feature maps $\{f_v^l \in \mathbb{R}^{C^l \times H^l \times W^l}\}_{l=1}^4$, where C^l , H^l and W^l denote the channel dimension, height, and width of the feature map at the l^{th} level, respectively. F_p is a set of word-level embeddings $\{f_p^i \in \mathbb{R}^{len_i \times C}\}_{i=1}^{N_p}$, where len_i and C denote the sentence length and channel dimension of the i^{th} prompt, respectively.

Cross-modal Prompt Fusion. Having obtained the visual and textual features, we proceed with Cross-modal Prompt Fusion. This module enhances the focus on target objects within images by leveraging text prompts and assists in selecting the most relevant and useful prompt for each specific clip. The process involves three key steps. 1) For features of each image, we first apply Multi-Head Attention (MHA) mechanisms between the visual feature maps at the last three levels and the word-level embeddings from the text prompts. Each text prompt leads to corresponding proposals, denoted as \mathbb{A} , \mathbb{B} , \mathbb{C} , respectively. This allows us to capture intricate relationships between the visual and textual data. 2) Our goal is to identify the target object, i.e. $\mathbb{A} \cap \mathbb{B} \cap \mathbb{C}$. The attention output is then flattened and passed through a three-layer Multi-Layer Perceptron (MLP) to compute weights for each text prompt. These weights reflect the relevance of each prompt to the current clip. Using the computed weights, we perform a weighted sum of the attention output to obtain the fused visual features. This step integrates the most pertinent aspects of the text prompts with the visual data. The process can be formulated as:

$$A^{l,i} = \text{MHA}(f_v^l, f_p^i), \quad (1)$$

$$W^{l,i} = \text{Softmax}(\text{MLP}(A^{l,i})), \quad (2)$$

$$F'_v = \left\{ \sum_{i=1}^{N_p} f_v^l \cdot A^{l,i} \cdot W^{l,i} \right\}_{l=2}^4. \quad (3)$$

3) For the textual features, we select the prompt with the highest weight score produced by the feature maps at the first level ($l = \{1\}$). The textual feature of this prompt is then fed into the Transformer decoder as the query input.

$$\hat{w} = \arg \max_{i \in \{1, \dots, N_p\}} (W^{l=1,i}), \quad (4)$$

$$F'_p = f_p^{\hat{w}}. \quad (5)$$

3.2 UNIFIED SEQUENTIAL PROCESSING

Transformer. Our Transformer architecture is adapted from Deformable DETR. For each image I_t , the Transformer encoder takes the flattened visual features $F'_{v,t}$ and 2D positional encoding as input, producing encoded output $E_{v,t}$ through multi-scale deformable attention and several feed forward layers. The output of the Transformer encoder $E_{v,t}$ and the textual feature of the selected prompt $F'_{p,t}$ are then fed into the Transformer decoder. We repeat $F'_{p,t}$ N_q times to introduce N_q queries, denoted as q_t . Meanwhile, each image receives sequential cues from the previous frame (except for the first image) in temporal order. The Transformer decoder thus generates N_q embeddings for each image, denoted as q_t^{embed} .

Prediction Heads. Three prediction heads are constructed following the Transformer decoder. The output embeddings from the Transformer decoder, q_t^{embed} , are then processed by these prediction heads. 1) The **box head** consists of a three-layer feed-forward network (FFN) with ReLU activation, except for the last layer, which predicts the box offset. The offset is added to the base box coordinates to determine the location of the referred object, denoted as b_t . 2) The **mask head** is implemented by dynamic convolution (Tian et al., 2020). It takes multi-scale features from the feature pyramid network (FPN) f_m , concatenates them with relative coordinates, and uses a controller to generate convolutional parameters θ_t . Conditional convolution is then applied to the visual features to generate N_q segmentation masks m_t .

$$\theta_t = \text{Controller}(q_t^{embed}), \quad (6)$$

$$\{m_t^i\}_{i=1}^{N_q} = \{\phi^i(f_m; \theta_t^i)\}_{i=1}^{N_q}. \quad (7)$$

Here, the controller is also a three-layer FFN with ReLU activation, except for the last layer, and ϕ^i represents three 1×1 convolutional layers with 8 channels per query, using parameters θ_t^i generated by the controller. 3) Since our text prompts contain class information, the **class head** indicates whether the object is referred by the text prompt.

Triple Propagation. Frames or slices in temporal order across a sequence of medical images often exhibit consistency in appearance or spatial relationships. To take advantage of this temporal coherence, we propagate the box, mask, and query embeddings derived from the previous image to assist in the prediction for the current image, as depicted in Figure 3 (b). This triple propagation leverages the temporal consistency within the sequence, enhancing the robustness and precision of medical image sequence analysis and ultimately contributing to more reliable outcomes.

Given the outputs of the previous image $y_{t-1} = \{b_{t-1}^i, m_{t-1}^i, c_{t-1}^i\}_{i=1}^{N_q}$, we first choose the prediction with highest class score as the best prediction: $\{b_{t-1}^{\hat{n}}, m_{t-1}^{\hat{n}}, c_{t-1}^{\hat{n}}\}$. Consequently, except for the first image, which has N_q queries, subsequent images will contain only one query, as it is always propagated from the best prediction of the previous image.

Box-level Propagation. The box coordinates from the previous image $b_{t-1}^{\hat{n}}$ provide a valuable reference for estimating the location of the target object in the current image. We use these coordinates as the initial box for the current image, i.e. b_t^{base} , leveraging the spatial continuity between images to more accurately predict the object’s position. Box-level propagation allows us to refine the object’s localization by starting from a well-informed estimate.

Mask-level Propagation. Similarly, the visual features encoded by the Transformer encoder $E_{v,t-1}$ and the segmentation mask $m_{t-1}^{\hat{n}}$ from the previous image contains essential semantic information that can significantly aid in analyzing the current image. To effectively utilize this prior knowledge, we employ a memory-read mechanism inspired by Space-Time Memory (Oh et al., 2019). The difference is that we only generate key and value maps for the memory. The memory map M_{t-1} is a concatenation of $m_{t-1}^{\hat{n}}$ and the first level of $E_{v-1,t}$, and the memory read operation is defined as:

$$M_{t-1} = \text{Concat} (m_{t-1}^{\hat{n}}, E_{v,t-1}^{l=2}), \quad (8)$$

$$K = \psi (M_{t-1}), V = \varphi (M_{t-1}), \quad (9)$$

$$E_{v,t}^{l=2} = \text{Softmax} \left(\frac{E_{v,t}^{l=2} K}{\sqrt{C^{l=2}}} \right) V, \quad (10)$$

where ψ and φ are two parallel 3×3 convolutional layers. The first level of $E_{v,t}$ is now a memory-read map. It is concatenated with feature maps of other levels and then fed into the deformable attention module in the Transformer decoder after flattening.

Query-level Propagation. Having confirmed the query index \hat{n} , we propagate the corresponding output query embedding q_{t-1}^{embed} to the current image. Here, we use a three-layer FFN to transform the embedding to q_t , following (Wu et al., 2023). The propagation of the query allows for the transmission of embedded context for the same target.

3.3 TRAINING AND INFERENCE

Training. For each image, we have N_q predictions $y_t = \{b_t^i, m_t^i, c_t^i\}_{i=1}^{N_q}$, where $b_t^i \in \mathbb{R}^4$, $m_t^i \in \mathbb{R}^{\frac{H}{4} \times \frac{W}{4}}$, and $c_t^i \in \mathbb{R}^1$ represent the box location, segmentation mask, and probability of the referred object, respectively. The ground-truth, in the same format, is denoted as $Y_t = \{B_t, M_t, C_t\}$. We then compute the matching loss \mathcal{L}_{match} to find the best prediction:

$$\mathcal{L}_{match,t} (y_t, Y_t) = \lambda_{box} \mathcal{L}_{box} (y_t, Y_t) + \lambda_{mask} \mathcal{L}_{mask} (y_t, Y_t) + \lambda_{cls} \mathcal{L}_{cls} (y_t, Y_t), \quad (11)$$

$$\hat{n}_{q,t} = \arg \min_{i \in \{1, \dots, N_q\}} (\mathcal{L}_{match,t}), \quad (12)$$

where λ_{box} , λ_{mask} , and λ_{cls} are loss coefficients. \mathcal{L}_{box} is implemented as a sum of L1 loss and GIoU loss, \mathcal{L}_{mask} combines Dice loss and binary mask focal loss, and \mathcal{L}_{cls} is focal loss. $\hat{n}_{q,t}$ represents the query index of the best prediction. The network is optimized by minimizing the summation of $\mathcal{L}_{match,t}$ for the best predictions across T images.

$$\mathcal{L} = \frac{1}{T} \sum_{t=1}^T \mathcal{L}_{match,t}^{\hat{n}_{q,t}}. \quad (13)$$

Inference. During inference, we select the query with the highest class score as the best prediction, which can be formulated as:

$$\hat{n}'_{q,t} = \arg \max_{i \in \{1, \dots, N_q\}} (c_t^i). \quad (14)$$

The final segmentation masks for each image $\{\hat{m}_t\}_{t=1}^T$ are selected using the query index $\hat{n}'_{q,t}$ from the N_q predictions $\{m_t^i\}_{i=1}^{N_q}$. Due to our propagation strategy, the best prediction of the first image is propagated to the subsequent images, leading to only one query for the rest images. Therefore, for those images with only one query, $\hat{m}_t = m_t$ ($t > 1$).

4 EXPERIMENTS

4.1 DATASETS AND METRICS

Datasets and Metrics. We have collected and processed 18 medical image sequence datasets, including 20 anatomical entities across 4 different imaging modalities, as shown in Figure 2 and Table 1. The datasets are categorized by the 4 modalities as follows: 1) MRI datasets. 2018 Atria Segmentation Data (Xiong et al., 2021), RVSC (Petitjean et al., 2015), ACDC (Bernard et al.,

Table 1: Medical image sequence datasets across 4 modalities and 20 anatomical entities.

Dataset	Class	Type	Modality	Training cases (images)	Testing cases (images)
Xiong et al. (2021)	Left atrium	Organ	MRI	100 (5817)	54 (3202)
RVSC	Right ventricle	Organ	MRI	16 (243)	32 (514)
ACDC	Left ventricle Myocardium Right ventricle	Organ	MRI	100 (1808) 100 (1828) 100 (1558)	50 (977) 50 (989) 50 (881)
CAMUS	Left ventricle Myocardium Left atrium	Organ	Ultrasound	450 (8393)	50 (875)
Kiser et al. (2020)	Left lung Right lung	Organ	CT	300 (23858) 300 (24026)	98 (7931) 98 (7962)
Simpson et al. (2015)	Spleen	Organ	CT	30 (832)	11 (219)
Pancreas-CT	Pancreas	Organ	CT	60 (5158)	20 (1724)
BTCV	Aorta Left kidney Right kidney Liver Spleen Stomach Pancreas Gallbladder	Organ	CT	18 (1215) 18 (543) 18 (547) 18 (911) 18 (532) 18 (594) 18 (430) 17 (228)	12 (827) 12 (362) 12 (350) 12 (631) 12 (332) 12 (421) 12 (316) 11 (131)
Jiang et al. (2024)	Prostate	Organ	Ultrasound	55 (1931)	20 (690)
BraTS 2019	Brain tumor	Lesion	MRI	250 (16535)	85 (5613)
Zhang et al. (2023)	Breast mass	Lesion	MRI	80 (2913) 3 (39)	20 (565) 1 (32)
RIDER	Liver tumor	Lesion	CT	20 (703)	12 (1110)
LiTS	Liver tumor	Lesion	CT	20 (703)	12 (1110)
KiTS 2023	Kidney tumor	Lesion	CT	285 (4659)	40 (1110)
CVC-ClinicDB	Polyp	Lesion	Endoscopy	18 (367)	11 (245)
CVC-ColonDB				6 (180)	6 (120)
ETIS				20 (152)	6 (44)
ASU-Mayo				8 (2701)	2 (1155)

2018), BraTS 2019 (Menze et al., 2014; Bakas et al., 2017; Baid et al., 2021), Breast Cancer DCE-MRI Data (Zhang et al., 2023), and RIDER (Meyer et al., 2015). 2) CT datasets. Thoracic cavity segmentation dataset introduced by (Aerts et al., 2019), spleen segmentation dataset introduced by (Simpson et al., 2015), Pancreas-CT (Roth et al., 2015), the abdomen part of BTCV (Landman et al., 2015), LiTS (Bilic et al., 2023), and KiTS 2023 (Heller et al., 2021; 2023), 3) Ultrasound datasets. CAMUS (Leclerc et al., 2019), which is also known as echocardiography, and Micro-Ultrasound Prostate Segmentation Dataset (Jiang et al., 2024). 4) Endoscopy datasets. CVC-ClinicDB (Bernal et al., 2015), CVC-ColonDB (Bernal et al., 2012), ETIS (Silva et al., 2014), and ASU-Mayo (Tajbakhsh et al., 2015). We maintain the original training and testing splits, and ensure that each sequence is only used in one split. Segmentation performance is evaluated using the Dice coefficient and Hausdorff distance as metrics.

4.2 IMPLEMENTATION DETAILS

For all datasets, we convert videos into frames and 3D volumes into 2D slices. Images without a valid object are filtered out. In total, 3,644 sequences are used in training and 1,061 sequences for testing. Data augmentation techniques include random horizontal flip, random resize, random crop, and photometric distortion. All images are resized to a maximum length of 640 pixels. The coefficients for the losses are set as $\lambda_{L1} = 5$, $\lambda_{giou} = 2$, $\lambda_{dice} = 5$, $\lambda_{focal} = 2$, and $\lambda_{cls} = 2$. We adopt 4 encoder layers and 4 decoder layers in the Transformer, and the initial query number N_q is set to 5. Both the hidden dimension of the Transformer and the channel dimension of text prompts are $C = 256$. During training, 3 temporal images from a sequence are randomly sampled and fed into the model at each iteration. Our model is trained on 2 RTX 3090 24GB GPUs with a batch size of 1 per GPU, using AdamW optimizer with an initial learning rate of 10^{-5} for 5 epochs. The learning rate decays by 0.1 at the 3rd epoch.

Table 2: Comparison results with state-of-the-art methods on organs. \uparrow denotes higher is better and \downarrow denotes lower is better. Numbers in **bold** represent the best and underlined ones are the second best. ¹Average of ACDC and CAMUS, ²Average of left lung and right lung, ³Average of BTCV, Pancreas-CT, and Spleen segmentation dataset (Simpson et al., 2015).

Method	Backbone	Heart ¹		Lung ²		Abdomen ³		Prostate		Overall	
		Dice \uparrow	HD \downarrow	Dice \uparrow	HD \downarrow	Dice \uparrow	HD \downarrow	Dice \uparrow	HD \downarrow	Dice \uparrow	HD \downarrow
URVOS	ResNet-50	83.92	3.87	84.61	5.64	60.19	4.64	91.92	10.48	73.07	4.72
ReferFormer	ResNet-50	86.29	3.92	84.19	5.03	72.12	4.21	89.79	11.30	79.51	4.51
OnlineRefer	ResNet-50	83.93	3.94	85.27	4.89	63.48	4.59	91.69	10.98	74.69	4.68
Ours	ResNet-50	87.19	3.79	88.77	4.04	72.80	4.07	93.13	<u>10.75</u>	80.77	4.28
ReferFormer	Swin-L	84.12	3.99	82.56	5.12	66.05	4.31	90.58	11.26	75.67	4.60
OnlineRefer	Swin-L	84.37	3.90	83.59	4.99	60.39	4.62	90.72	10.80	73.30	4.68
Ours	Swin-L	84.47	3.87	84.96	4.99	66.41	<u>4.52</u>	91.54	<u>10.93</u>	76.25	4.62
SOC	V-Swin-T	81.76	4.22	84.84	4.94	62.55	4.82	86.42	12.73	73.12	4.98
MTTR	V-Swin-T	84.80	3.98	84.92	4.94	64.23	4.39	89.96	11.95	75.26	4.65
Ours	V-Swin-T	84.98	3.85	85.19	4.93	65.57	4.31	92.34	10.70	76.11	4.50

Table 3: Comparison results with state-of-the-art methods on lesions. ¹Average of Breast Cancer DCE-MRI Data and RIDER. ²Average of CVC-ClinicDB, CVC-ColonDB, ETIS, and ASU-Mayo.

Method	Backbone	Brain tumor		Breast mass ¹		Liver tumor		Kidney tumor		Polyp ²	
		Dice \uparrow	HD \downarrow	Dice \uparrow	HD \downarrow	Dice \uparrow	HD \downarrow	Dice \uparrow	HD \downarrow	Dice \uparrow	HD \downarrow
URVOS	ResNet-50	74.59	4.73	55.91	5.20	27.43	8.51	72.24	5.63	66.17	7.79
ReferFormer	ResNet-50	76.60	3.16	60.70	4.93	47.43	8.97	61.75	6.83	62.75	8.19
OnlineRefer	ResNet-50	77.55	3.00	64.81	4.48	39.70	8.85	74.75	5.58	72.77	7.31
Ours	ResNet-50	78.24	2.96	65.40	<u>4.66</u>	65.27	6.82	77.73	5.56	75.56	7.07
ReferFormer	Swin-L	76.89	3.06	61.53	4.78	57.43	7.48	78.31	5.46	67.35	7.81
OnlineRefer	Swin-L	77.46	2.97	57.22	4.62	54.50	7.57	69.91	6.04	78.47	6.80
Ours	Swin-L	77.96	<u>3.03</u>	65.90	4.49	59.32	7.45	79.27	5.26	<u>77.56</u>	<u>7.25</u>
SOC	V-Swin-T	75.55	3.05	61.57	4.75	35.30	8.42	70.01	6.08	60.04	8.73
MTTR	V-Swin-T	76.21	3.00	57.74	4.95	53.68	7.28	67.31	6.33	71.12	7.72
Ours	V-Swin-T	77.37	2.98	<u>59.17</u>	4.52	54.26	8.55	76.07	5.61	77.11	6.93

4.3 RESULTS

Comparison to the State-of-the-art. We compare our method with state-of-the-art approaches on referring video object segmentation, including URVOS (Seo et al., 2020), ReferFormer (Wu et al., 2022), OnlineRefer (Wu et al., 2023), MTTR (Botach et al., 2022), and SOC (Luo et al., 2024). The comparison results for organs and lesions are shown in Table 2 and Table 3, respectively. To better organize and present the datasets, we categorize the organ datasets into four distinct groups: heart, lung, abdomen, and prostate. We then compute the average metrics for each group, allowing us to identify strengths and weaknesses specific to different anatomical regions.

For feature extraction, we implement various visual backbones, including ResNet (He et al., 2016), Swin Transformer (Liu et al., 2021), and Video Swin Transformer (Liu et al., 2022). Notably, the performance for organ detection is superior to that for lesion detection. This discrepancy can be attributed to the smaller size and more homogeneous appearance of lesions, which makes them inherently more challenging to identify. Our approach consistently outperforms previous methods across all three backbones, especially on lesion datasets. For the segmentation of liver tumors and kidney tumors, our model with a ResNet-50 backbone achieves average Dice scores of 65.27% and 77.73%, which are 17.84 and 15.98 points higher than the previous state-of-the-art work, ReferFormer. Figure 5 shows the visualization results of our TPP.

Comparison to SAM 2. The Segment Anything Model 2 (Ravi et al., 2024) serves as a foundational model for promptable visual segmentation in images and videos. As it currently lacks support for text prompts, we utilize a community-developed version, Grounded SAM 2 (Liu et al., 2023), which enables video object tracking with text inputs. This model uses box outputs from Grounding DINO as prompts for SAM 2’s video predictor. Despite this integration, it achieves average Dice scores

Table 4: Comparison with SAM 2 series.

Prompter + Segmenter	Metric	Organ	Lesion
Grounding DINO	Dice↑	12.46	10.10
	HD↓	17.08	21.05
TPP	Dice↑	53.45	54.55
	HD↓	6.03	6.79
TPP + TPP	Dice↑	80.77	72.69
	HD↓	4.28	5.88

Table 5: Few-shot performance.

Method	Metric	Right ventricle	Breast mass	Polyp
Full data	Dice↑	81.97	61.96	82.19
	HD↓	3.45	4.57	6.65
One-shot	Dice↑	75.63	59.88	81.55
	HD↓	3.93	4.56	6.65
Zero-shot	Dice↑	71.13	57.18	80.97
	HD↓	4.29	4.60	6.70

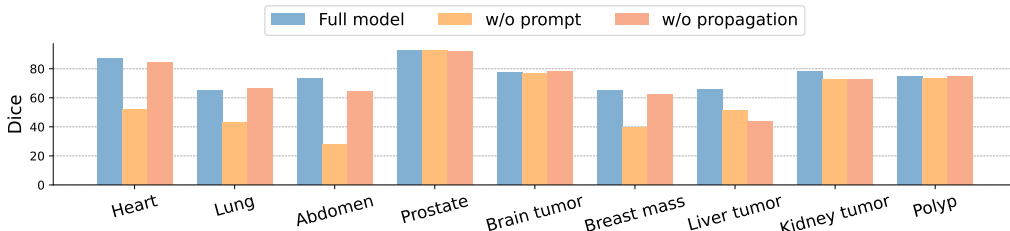


Figure 4: Ablation studies on text prompts and propagation strategies. Dice scores are provided for full model, without prompt, and without propagation, respectively.

of only 12.46% for organs and 10.10% for lesions, indicating its limited understanding of medical text prompts. To address this, we utilize the mask predictions of the first image in the sequences generated by our TPP as mask prompts for SAM 2, which leads to substantial improvements, with average Dice scores of 53.45% (+40.99) for organs and 54.55% (+44.45) for lesions. As shown in Table 4, our TPP demonstrates superiority over Grounding DINO in text grounding ability, and surpasses SAM 2 in object tracking capabilities due to the triple propagation strategy.

Zero-/Few-shot Performance. To validate the zero-shot performance of our approach on unseen datasets, we exclude RVSC (right ventricle), RIDER (breast mass), and CVC-ColonDB (polyp) from the training datasets and evaluate the trained model on these datasets directly. As shown in Table 5, the Dice scores for breast mass and polyp decrease by only 4.78 and 1.22 points compared to full-data training. In the one-shot setting, we use a single sequence from each of the three datasets mentioned above for training. The results show that one-shot performance is comparable to full-data training, highlighting the model’s robust generalization ability.

4.4 ABLATION STUDY

Cross-modal prompt fusion and the propagation strategy are critical components of our approach to referring medical image sequence segmentation. Figure 4 illustrates that medical text prompts are particularly essential for accurately identifying organs located in the heart, lungs, and abdomen. Moreover, for extremely small lesions, such as breast masses and liver tumors, our propagation strategy significantly reduces the occurrence of false negatives, resulting in significant enhancements.

Medical Text Prompts. We utilize large language models to generate three attributes for each anatomical entity: [profile], [color], and [shape]. Among these, [profile] is a more abstract concept,

Table 6: Ablation studies on prompts.

Prompt	Organ		Lesion	
	Dice↑	HD↓	Dice↑	HD↓
w/o prompt	41.45	8.14	63.69	6.55
w/ [profile]	76.17	4.71	66.07	6.18
w/ [color] & [shape]	78.31	4.70	67.50	6.34
Full model	80.77	4.28	72.69	5.88

Table 7: Ablation studies on propagation.

Propagation	Organ		Lesion	
	Dice↑	HD↓	Dice↑	HD↓
w/o prop.	74.53	4.75	63.97	6.51
w/o query	77.86	4.66	64.03	6.42
w/o mask	77.93	4.61	67.10	6.40
w/o box	79.57	4.48	71.43	6.05
Full model	80.77	4.28	72.69	5.88

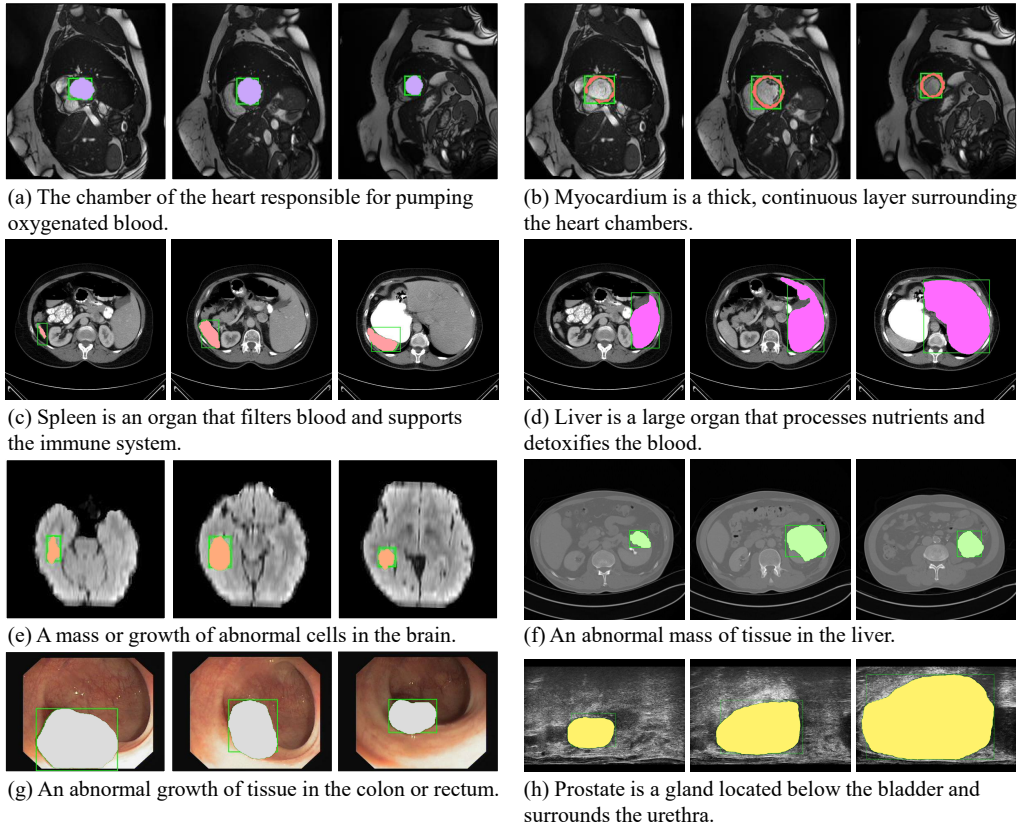


Figure 5: Visualization of segmentation results for different entities and modalities. (a) and (b) display the results of left atrium and myocardium in the same MRIs, respectively. (c) and (d) show spleen and liver in the same CT slices, respectively. From (e) to (h), visualizations are brain tumor in MRI, liver tumor in CT, polyp in endoscopy, and prostate in ultrasound.

whereas [color] and [shape] are more specific. These different attributes serve as varied prompt messages, resulting in distinct enhancements in segmentation performance, as shown in Table 6.

Propagation Strategy. To investigate the effects of box propagation, mask propagation, and query propagation, we conduct ablation experiments by removing the corresponding propagation methods, as demonstrated in Table 7. The absence of mask propagation and query propagation results in decreases of 2.84 and 2.91 points in Dice score, and increases of 0.33 and 0.38 in HD for organs.

5 CONCLUSION

In this paper, we introduce a new task, termed Referring Medical Image Sequence Segmentation, accompanied by a large and comprehensive benchmark. The benchmark includes 20 different anatomical entities across 4 modalities from various regions of the body. We present an innovative text-promptable approach that effectively leverages the inherent sequential relationships and textual cues within medical image sequences to segment referred objects, serving as a strong baseline for this task. By integrating both 2D and 3D medical images through a triple-propagation strategy, we demonstrate significant improvements across a broad spectrum of medical datasets, emphasizing the potential for rapid response in segmenting referred objects and enabling accurate diagnosis in clinical practice. Future work should delve deeper into optimizing prompts and exploring additional modalities to further enhance the efficacy of medical image analysis.

REFERENCES

- H. J. W. L. Aerts, L. Wee, E. Rios Velazquez, R. T. H. Leijenaar, C. Parmar, P. Grossmann, S. Carvalho, J. Bussink, R. Monshouwer, B. Haibe-Kains, D. Rietveld, F. Hoebbers, M. M. Rietbergen, C. R. Leemans, A. Dekker, J. Quackenbush, R. J. Gillies, and P. Lambin. Data from nscl-radiomics (version 4). Data set, 2019. URL <https://doi.org/10.7937/K9/TCIA.2015.PF0M9REI>.
- Ujjwal Baid, Satyam Ghodasara, Suyash Mohan, Michel Bilello, Evan Calabrese, Errol Colak, Keyvan Farahani, Jayashree Kalpathy-Cramer, Felipe C Kitamura, Sarthak Pati, et al. The rsna-asnr-miccai brats 2021 benchmark on brain tumor segmentation and radiogenomic classification. *arXiv preprint arXiv:2107.02314*, 2021.
- Spyridon Bakas, Hamed Akbari, Aristeidis Sotiras, Michel Bilello, Martin Rozycki, Justin S Kirby, John B Freymann, Keyvan Farahani, and Christos Davatzikos. Advancing the cancer genome atlas glioma mri collections with expert segmentation labels and radiomic features. *Scientific data*, 4(1):1–13, 2017.
- Shruthi Bannur, Stephanie Hyland, Qianchu Liu, Fernando Perez-Garcia, Maximilian Ilse, Daniel C Castro, Benedikt Boecking, Harshita Sharma, Kenza Bouzid, Anja Thieme, et al. Learning to exploit temporal structure for biomedical vision-language processing. In *Proceedings of the IEEE/CVF Conference on Computer Vision and Pattern Recognition*, pp. 15016–15027, 2023.
- Jorge Bernal, Javier Sánchez, and Fernando Vilarino. Towards automatic polyp detection with a polyp appearance model. *Pattern Recognition*, 45(9):3166–3182, 2012.
- Jorge Bernal, F Javier Sánchez, Gloria Fernández-Esparrach, Debora Gil, Cristina Rodríguez, and Fernando Vilarino. Wm-dova maps for accurate polyp highlighting in colonoscopy: Validation vs. saliency maps from physicians. *Computerized medical imaging and graphics*, 43:99–111, 2015.
- Olivier Bernard, Alain Lalande, Clement Zotti, Frederick Cervenansky, Xin Yang, Pheng-Ann Heng, Irem Cetin, Karim Lekadir, Oscar Camara, Miguel Angel Gonzalez Ballester, et al. Deep learning techniques for automatic mri cardiac multi-structures segmentation and diagnosis: is the problem solved? *IEEE transactions on medical imaging*, 37(11):2514–2525, 2018.
- Patrick Bilic, Patrick Christ, Hongwei Bran Li, Eugene Vorontsov, Avi Ben-Cohen, Georgios Kaissis, Adi Szeskin, Colin Jacobs, Gabriel Efrain Humpire Mamani, Gabriel Chartrand, et al. The liver tumor segmentation benchmark (lits). *Medical Image Analysis*, 84:102680, 2023.
- Adam Botach, Evgenii Zheltonozhskii, and Chaim Baskin. End-to-end referring video object segmentation with multimodal transformers. In *Proceedings of the IEEE/CVF Conference on Computer Vision and Pattern Recognition*, pp. 4985–4995, 2022.
- Jieneng Chen, Yongyi Lu, Qihang Yu, Xiangde Luo, Ehsan Adeli, Yan Wang, Le Lu, Alan L Yuille, and Yuyin Zhou. Transunet: Transformers make strong encoders for medical image segmentation. *arXiv preprint arXiv:2102.04306*, 2021.
- Özgün Çiçek, Ahmed Abdulkadir, Soeren S Lienkamp, Thomas Brox, and Olaf Ronneberger. 3d u-net: learning dense volumetric segmentation from sparse annotation. In *International Conference on Medical Image Computing and Computer-Assisted Intervention, Part II 19*, pp. 424–432. Springer, 2016.
- Kirill Gavriluk, Amir Ghodrati, Zhenyang Li, and Cees GM Snoek. Actor and action video segmentation from a sentence. In *Proceedings of the IEEE conference on computer vision and pattern recognition*, pp. 5958–5966, 2018.
- Kaiming He, Xiangyu Zhang, Shaoqing Ren, and Jian Sun. Deep residual learning for image recognition. In *Proceedings of the IEEE conference on computer vision and pattern recognition*, pp. 770–778, 2016.

-
- Nicholas Heller, Fabian Isensee, Klaus H Maier-Hein, Xiaoshuai Hou, Chunmei Xie, Fengyi Li, Yang Nan, Guangrui Mu, Zhiyong Lin, Miofei Han, et al. The state of the art in kidney and kidney tumor segmentation in contrast-enhanced ct imaging: Results of the kits19 challenge. *Medical image analysis*, 67:101821, 2021.
- Nicholas Heller, Fabian Isensee, Dasha Trofimova, Resha Tejpaul, Zhongchen Zhao, Huai Chen, Lisheng Wang, Alex Golts, Daniel Khapun, Daniel Shats, et al. The kits21 challenge: Automatic segmentation of kidneys, renal tumors, and renal cysts in corticomedullary-phase ct. *arXiv preprint arXiv:2307.01984*, 2023.
- Chaoqin Huang, Aofan Jiang, Jinghao Feng, Ya Zhang, Xinchao Wang, and Yanfeng Wang. Adapting visual-language models for generalizable anomaly detection in medical images. In *Proceedings of the IEEE/CVF Conference on Computer Vision and Pattern Recognition*, pp. 11375–11385, 2024.
- Fabian Isensee, Paul F Jaeger, Simon AA Kohl, Jens Petersen, and Klaus H Maier-Hein. nnu-net: a self-configuring method for deep learning-based biomedical image segmentation. *Nature methods*, 18(2):203–211, 2021.
- Ge-Peng Ji, Yu-Cheng Chou, Deng-Ping Fan, Geng Chen, Huazhu Fu, Debesh Jha, and Ling Shao. Progressively normalized self-attention network for video polyp segmentation. In *International Conference on Medical Image Computing and Computer-Assisted Intervention*, pp. 142–152. Springer, 2021.
- Hongxu Jiang, Muhammad Imran, Preethika Muralidharan, Anjali Patel, Jake Pensa, Muxuan Liang, Tarik Benidir, Joseph R Grajo, Jason P Joseph, Russell Terry, et al. Microsegnet: A deep learning approach for prostate segmentation on micro-ultrasound images. *Computerized Medical Imaging and Graphics*, pp. 102326, 2024.
- Alexander Kirillov, Eric Mintun, Nikhila Ravi, Hanzi Mao, Chloe Rolland, Laura Gustafson, Tete Xiao, Spencer Whitehead, Alexander C Berg, Wan-Yen Lo, et al. Segment anything. In *Proceedings of the IEEE/CVF International Conference on Computer Vision*, pp. 4015–4026, 2023.
- K.J. Kiser, S. Ahmed, S.M. Stieb, A.S.R. Mohamed, H. Elhalawani, P.Y.S. Park, N.S. Doyle, B.J. Wang, A. Barman, C.D. Fuller, and L. Giancardo. Data from the thoracic volume and pleural effusion segmentations in diseased lungs for benchmarking chest ct processing pipelines (plethora). Data set, 2020. URL <https://doi.org/10.7937/tcia.2020.6c7y-gq39>.
- Bennett Landman, Zhoubing Xu, J Igelsias, Martin Styner, Thomas Langerak, and Arno Klein. Miccai multi-atlas labeling beyond the cranial vault—workshop and challenge. In *Proc. MICCAI Multi-Atlas Labeling Beyond Cranial Vault—Workshop Challenge*, volume 5, pp. 12, 2015.
- Sarah Leclerc, Erik Smistad, Joao Pedrosa, Andreas Østvik, Frederic Cervenansky, Florian Espinosa, Torvald Espeland, Erik Andreas Rye Berg, Pierre-Marc Jodoin, Thomas Grenier, et al. Deep learning for segmentation using an open large-scale dataset in 2d echocardiography. *IEEE transactions on medical imaging*, 38(9):2198–2210, 2019.
- Zihan Li, Yunxiang Li, Qingde Li, Puyang Wang, Dazhou Guo, Le Lu, Dakai Jin, You Zhang, and Qingqi Hong. Lvit: language meets vision transformer in medical image segmentation. *IEEE transactions on medical imaging*, 2023.
- Junhao Lin, Qian Dai, Lei Zhu, Huazhu Fu, Qiong Wang, Weibin Li, Wenhao Rao, Xiaoyang Huang, and Liansheng Wang. Shifting more attention to breast lesion segmentation in ultrasound videos. In *International Conference on Medical Image Computing and Computer-Assisted Intervention*, pp. 497–507. Springer, 2023.
- Shilong Liu, Zhaoyang Zeng, Tianhe Ren, Feng Li, Hao Zhang, Jie Yang, Chunyuan Li, Jianwei Yang, Hang Su, Jun Zhu, et al. Grounding dino: Marrying dino with grounded pre-training for open-set object detection. *arXiv preprint arXiv:2303.05499*, 2023.
- Ze Liu, Yutong Lin, Yue Cao, Han Hu, Yixuan Wei, Zheng Zhang, Stephen Lin, and Baining Guo. Swin transformer: Hierarchical vision transformer using shifted windows. In *Proceedings of the IEEE/CVF international conference on computer vision*, pp. 10012–10022, 2021.

-
- Ze Liu, Jia Ning, Yue Cao, Yixuan Wei, Zheng Zhang, Stephen Lin, and Han Hu. Video swin transformer. In *Proceedings of the IEEE/CVF conference on computer vision and pattern recognition*, pp. 3202–3211, 2022.
- Ming Y Lu, Bowen Chen, Andrew Zhang, Drew FK Williamson, Richard J Chen, Tong Ding, Long Phi Le, Yung-Sung Chuang, and Faisal Mahmood. Visual language pretrained multiple instance zero-shot transfer for histopathology images. In *Proceedings of the IEEE/CVF conference on computer vision and pattern recognition*, pp. 19764–19775, 2023.
- Zhuoyan Luo, Yicheng Xiao, Yong Liu, Shuyan Li, Yitong Wang, Yansong Tang, Xiu Li, and Yujiu Yang. Soc: Semantic-assisted object cluster for referring video object segmentation. *Advances in Neural Information Processing Systems*, 36, 2024.
- Bjoern H Menze, Andras Jakab, Stefan Bauer, Jayashree Kalpathy-Cramer, Keyvan Farahani, Justin Kirby, Yuliya Burren, Nicole Porz, Johannes Slotboom, Roland Wiest, et al. The multimodal brain tumor image segmentation benchmark (brats). *IEEE transactions on medical imaging*, 34(10):1993–2024, 2014.
- C. R. Meyer, T. L. Chenevert, C. J. Galbán, T. D. Johnson, D. A. Hamstra, A. Rehemtulla, and B. D. Ross. Rider breast mri. Data set, 2015. URL <https://doi.org/10.7937/K9/TCIA.2015.H1SXNUXL>.
- Fausto Milletari, Nassir Navab, and Seyed-Ahmad Ahmadi. V-net: Fully convolutional neural networks for volumetric medical image segmentation. In *2016 fourth international conference on 3D vision (3DV)*, pp. 565–571. Ieee, 2016.
- Jong Hak Moon, Hyungyung Lee, Woncheol Shin, Young-Hak Kim, and Edward Choi. Multi-modal understanding and generation for medical images and text via vision-language pre-training. *IEEE Journal of Biomedical and Health Informatics*, 26(12):6070–6080, 2022.
- Michael Moor, Qian Huang, Shirley Wu, Michihiro Yasunaga, Yash Dalmia, Jure Leskovec, Cyril Zakka, Eduardo Pontes Reis, and Pranav Rajpurkar. Med-flamingo: a multimodal medical few-shot learner. In *Machine Learning for Health (ML4H)*, pp. 353–367. PMLR, 2023.
- Seoung Wug Oh, Joon-Young Lee, Ning Xu, and Seon Joo Kim. Video object segmentation using space-time memory networks. In *Proceedings of the IEEE/CVF international conference on computer vision*, pp. 9226–9235, 2019.
- Nathan Painchaud, Nicolas Duchateau, Olivier Bernard, and Pierre-Marc Jodoin. Echocardiography segmentation with enforced temporal consistency. *IEEE Transactions on Medical Imaging*, 41(10):2867–2878, 2022.
- Caroline Petitjean, Maria A Zuluaga, Wenjia Bai, Jean-Nicolas Dacher, Damien Grosgeorge, Jérôme Caudron, Su Ruan, Ismail Ben Ayed, M Jorge Cardoso, Hsiang-Chou Chen, et al. Right ventricle segmentation from cardiac mri: a collation study. *Medical image analysis*, 19(1):187–202, 2015.
- Ziyuan Qin, Hua Hui Yi, Qicheng Lao, and Kang Li. MEDICAL IMAGE UNDERSTANDING WITH PRETRAINED VISION LANGUAGE MODELS: A COMPREHENSIVE STUDY. In *The Eleventh International Conference on Learning Representations*, 2023.
- Nikhila Ravi, Valentin Gabeur, Yuan-Ting Hu, Ronghang Hu, Chaitanya Ryali, Tengyu Ma, Haitham Khedr, Roman Rädle, Chloe Rolland, Laura Gustafson, Eric Mintun, Junting Pan, Kalyan Vasudev Alwala, Nicolas Carion, Chao-Yuan Wu, Ross Girshick, Piotr Dollár, and Christoph Feichtenhofer. Sam 2: Segment anything in images and videos. *arXiv preprint arXiv:2408.00714*, 2024.
- Olaf Ronneberger, Philipp Fischer, and Thomas Brox. U-net: Convolutional networks for biomedical image segmentation. In *International Conference on Medical Image Computing and Computer-Assisted Intervention, part III 18*, pp. 234–241. Springer, 2015.
- Holger R Roth, Le Lu, Amal Farag, Hoo-Chang Shin, Jiamin Liu, Evrim B Turkbey, and Ronald M Summers. Deeporgan: Multi-level deep convolutional networks for automated pancreas segmentation. In *International Conference on Medical Image Computing and Computer-Assisted Intervention, Part I 18*, pp. 556–564. Springer, 2015.

-
- Seonguk Seo, Joon-Young Lee, and Bohyung Han. Urvos: Unified referring video object segmentation network with a large-scale benchmark. In *Computer Vision–ECCV 2020: 16th European Conference, Glasgow, UK, August 23–28, 2020, Proceedings, Part XV 16*, pp. 208–223. Springer, 2020.
- Juan Silva, Aymeric Histace, Olivier Romain, Xavier Dray, and Bertrand Granado. Toward embedded detection of polyps in wce images for early diagnosis of colorectal cancer. *International journal of computer assisted radiology and surgery*, 9:283–293, 2014.
- Amber L Simpson, Julie N Leal, Amudhan Pugalenth, Peter J Allen, Ronald P DeMatteo, Yuman Fong, Mithat Gönen, William R Jarnagin, T Peter Kingham, Michael I Miga, et al. Chemotherapy-induced splenic volume increase is independently associated with major complications after hepatic resection for metastatic colorectal cancer. *Journal of the American College of Surgeons*, 220(3):271–280, 2015.
- Karan Singhal, Shekoofeh Azizi, Tao Tu, S Sara Mahdavi, Jason Wei, Hyung Won Chung, Nathan Scales, Ajay Tanwani, Heather Cole-Lewis, Stephen Pfohl, et al. Large language models encode clinical knowledge. *Nature*, 620(7972):172–180, 2023.
- Nima Tajbakhsh, Suryakanth R Gurudu, and Jianming Liang. Automated polyp detection in colonoscopy videos using shape and context information. *IEEE transactions on medical imaging*, 35(2):630–644, 2015.
- Zhi Tian, Chunhua Shen, and Hao Chen. Conditional convolutions for instance segmentation. In *Computer Vision–ECCV 2020: 16th European Conference, Glasgow, UK, August 23–28, 2020, Proceedings, Part I 16*, pp. 282–298. Springer, 2020.
- Ekin Tiu, Ellie Talius, Pujan Patel, Curtis P Langlotz, Andrew Y Ng, and Pranav Rajpurkar. Expert-level detection of pathologies from unannotated chest x-ray images via self-supervised learning. *Nature Biomedical Engineering*, 6(12):1399–1406, 2022.
- Zifeng Wang, Zhenbang Wu, Dinesh Agarwal, and Jimeng Sun. MedCLIP: Contrastive learning from unpaired medical images and text. In *Proceedings of the 2022 Conference on Empirical Methods in Natural Language Processing*, pp. 3876–3887, December 2022.
- Dongming Wu, Tiancai Wang, Yuang Zhang, Xiangyu Zhang, and Jianbing Shen. Onlinerefer: A simple online baseline for referring video object segmentation. In *Proceedings of the IEEE/CVF International Conference on Computer Vision*, pp. 2761–2770, 2023.
- Jiannan Wu, Yi Jiang, Peize Sun, Zehuan Yuan, and Ping Luo. Language as queries for referring video object segmentation. In *Proceedings of the IEEE/CVF Conference on Computer Vision and Pattern Recognition*, pp. 4974–4984, 2022.
- Zhaohan Xiong, Qing Xia, Zhiqiang Hu, Ning Huang, Cheng Bian, Yefeng Zheng, Sulaiman Vesal, Nishant Ravikumar, Andreas Maier, Xin Yang, et al. A global benchmark of algorithms for segmenting the left atrium from late gadolinium-enhanced cardiac magnetic resonance imaging. *Medical image analysis*, 67:101832, 2021.
- Bin Yan and Mingtao Pei. Clinical-bert: Vision-language pre-training for radiograph diagnosis and reports generation. In *Proceedings of the AAAI Conference on Artificial Intelligence*, volume 36, pp. 2982–2990, 2022.
- Jiadong Zhang, Zhiming Cui, Zhenwei Shi, Yingjia Jiang, Zhiliang Zhang, Xiaoting Dai, Zhenlu Yang, Yuning Gu, Lei Zhou, Chu Han, et al. A robust and efficient ai assistant for breast tumor segmentation from dce-mri via a spatial-temporal framework. *Patterns*, 4(9), 2023.
- Xiangyu Zhao, Peng Zhang, Fan Song, Chenbin Ma, Guangda Fan, Yangyang Sun, Youdan Feng, and Guanglei Zhang. Prior attention network for multi-lesion segmentation in medical images. *IEEE Transactions on Medical Imaging*, 41(12):3812–3823, 2022.
- Ziheng Zhao, Yao Zhang, Chaoyi Wu, Xiaoman Zhang, Ya Zhang, Yanfeng Wang, and Weidi Xie. One model to rule them all: Towards universal segmentation for medical images with text prompts. *arXiv preprint arXiv:2312.17183*, 2023.